J. Iron Steel Res. Int.
https://doi.org/10.1007/s42243-024-01280-9

ORIGINAL PAPER

Microstructure evolution and mechanical properties improvement of $(Ti_8Zr_6Nb_4V_5Cr_4)_{100-x}Al_x$ lightweight high-entropy alloy by Laves phase transformation

Qin Xu[1] · Cheng-yuan Guo[1] · Qi Wang[2] · Peng-yu Sun[1] · Ya-jun Yin[3] · Rui-run Chen[2]

Received: 28 February 2024 / Revised: 15 April 2024 / Accepted: 16 April 2024

Abstract
$(Ti_8Zr_6Nb_4V_5Cr_4)_{100-x}Al_x$ (x = 0, 0.1, 0.2, 0.3, 0.4 at.%) lightweight high-entropy alloys with different contents of Al were prepared via vacuum non-consumable arc melting method. Effects of adding varying Al contents on phase constitution, microstructure characteristics and mechanical properties of the lightweight alloys were studied. Results show that $Ti_8Zr_6Nb_4V_5Cr_4$ alloy is composed of body-centered cubic (BCC) phase and C15 Laves phase, while $(Ti_8Zr_6Nb_4V_5Cr_4)_{100-x}Al_x$ lightweight high-entropy alloys by addition of Al are composed of BCC phase and C14 Laves phase. Addition of Al into $Ti_8Zr_6Nb_4V_5Cr_4$ lightweight high-entropy alloy can transform C15 Laves phase to C14 Laves phase. With further addition of Al, BCC phase of alloys is significantly refined, and the volume fraction of C14 Laves phase is raised obviously. Meanwhile, the dimension of BCC phase in the alloy by addition of 0.3 at.% Al is the most refined and that of Laves phase is also obviously refined. Adding Al to $Ti_8Zr_6Nb_4V_5Cr_4$ alloy can not only reduce the density of $(Ti_8Zr_6Nb_4V_5Cr_4)_{100-x}Al_x$ alloy, but also improve strength of $(Ti_8Zr_6Nb_4V_5Cr_4)_{100-x}Al_x$ alloy. As Al content increased from 0 to 0.4 at.%, the density of the alloy decreased from 6.22 ± 0.875 to 5.79 ± 0.679 g cm^{-3}. Moreover, compressive strength of the alloy by 0.3 at.% Al addition is the highest to 1996.9 MPa, while fracture strain of the alloy is 16.82%. Strength improvement of alloys mainly results from microstructure refinement and precipitation of C14 Laves by Al addition into $Ti_8Zr_6Nb_4V_5Cr_4$ lightweight high-entropy alloy.

Keywords Lightweight high-entropy alloy · Phase transformation · Microstructure · Mechanical property · Refinement · Strengthening

1 Introduction

High-entropy alloys (HEAs) contain multiple elements greater than or equal to 4, and the percentage of each element ranges from 5% to 35% [1]. The 'high entropy' of high-entropy alloys refers to the chemical or topological disorder on atomic scale. HEAs expand new perspectives to design of alloys [2–6]. Since it was first discovered in 2004, high-entropy alloys have attracted much attention owing to their superior mechanical properties, for instance, high strength, high hardness, and corrosion resistance [7–14]. Particularly, innovative design concepts and broad compositional space have got worldwide attention and have been explored extensively by researchers [15–17]. Among them, CoCrFeMnNi HEA and its variants exhibit low temperature toughness [18, 19], $AlFe_4Cr_3Ti$ [20], WNbMoTaV [21] and $NbMoTiVWSi_x$ [22] high-entropy alloys show great stability and mechanical properties, and WTaCrV [23] exhibits excellent radiation resistance. However, there is a common disadvantage of high density [24], which greatly limits the application in the field of transportation. Obviously, lightweight materials will be a trend in the transportation field.

✉ Rui-run Chen
ruirunchen@hit.edu.cn

1 School of Mechanic and Electrical Engineering, Henan University of Technology, Zhengzhou 450001, Henan, China

2 National Key Laboratory for Precision Hot Processing of Metals, Harbin Institute of Technology, Harbin 150001, Heilongjiang, China

3 State Key Laboratory of Materials Processing and Die and Mould Technology, Huazhong University of Science and Technology, Wuhan 430074, Hubei, China

Published online: 06 August 2024

With the rapid transformation in the automotive industry and the higher step of energy saving and emission reduction for lightweighting, the demand and development of lightweight structural components have also changed [25–28]. The concept of high entropy gives brand-new ways for the development of lightweight alloys. Developing lighter weight materials with excellent performance has always been pursued by scientists. Scholars have continuously designed more lightweight high-entropy alloys (LHEAs) and studied their phase composition and mechanical properties. In our daily life, lightweight high-entropy alloys can leverage their advantages of lightweight and high strength to replace structural panels, seat frames, gearbox hubs, and other components in automobiles. Thus, LHEAs can effectively reduce vehicle weight, save oil consumption of traditional automobiles, and improve the endurance of new energy vehicles. As is well known, LHEAs can be distinguished into two types. The first one is designed by rational screening from lightweight elements like V, Al, Li, Ti, Mg, Si, Sc, Be, Sn, etc. [15, 24, 29]. Some of these alloys have extremely low density, between 1 and 4.5 g cm^{-3}. The case in point is LHEAs $Mg_x(MnAlZnCu)_{100-x}$ [30], AlLiMgSiGa [31], AlLiMgZnCu [32] and $Zr_{1.2}V_{0.8}Nb(Ti_xAl_y)$ [33] reported by researchers. In addition, some results show that excessive difference in atomic radius leads to mismatch of atomic radius and too low enthalpy between components, which will cause these alloys to form intermetallic compounds, ordered phases, and various brittle precipitates, and thus the investigation of alloy mechanical properties has been highly limited. Correspondingly, the second category of lightweight high-entropy alloy is designed on account of the existing high-entropy alloy solid solution, thus obtaining an LHEA with a solid solution phase as the composition phase.

Moreover, phase structure of lightweight high-entropy alloys is relatively simple. According to reports, addition of Al element into refractory high-entropy alloys (RHEAs) is an effective strategy to obtain ultra-high specific strength alloys with body-centered cubic (BCC) structure. However, as Al concentration increases, the primary structure changes from BCC to B2 represent disordered to ordered, leading to poor ductility. There is a circumstance of transformation from B2 to BCC phase, which is living the high aluminum content lightweight refractory high-entropy alloy $Zr_{40}Ti_{28}Nb_{12}Al_{20}$ [34]. The transformation is driven by the consumption of Al and Zr atoms in the solution during the precipitation of Al-rich B2 phase, leading to gradual formation of disordered BCC phase from B2 phase in matrix alloy, and ultimately transforming a BCC phase matrix with a single structure, which enhances tensile and ductile properties of the alloy while still maintaining a high degree of ductility. Qiu et al. [35] discovered that the lightweight high-entropy alloy AlTiVCr possesses single-phase B2 structure. B2 phase is more stable than BCC phase, attributed to lower formation enthalpy at low temperatures. In addition, a series of LHEAs TiZrVNbAl with BCC as the main phase was designed by taking the weighty elements Hf and Ta in the high-entropy alloy TiZrHfNbTa by the lighter elements V and Al [36, 37]. Scholars have adopted the same design concept to design LHEAs with single/main BCC phase or BCC/B2 phase, like $Ti_x(AlCrNb)_{100-x}$ [38], $Ti_{1.6}ZrNbAl_x$ [39], $TiZrV_{0.5}Nb_{0.5}$ [40], $Al_xCrNbTiVZr$ [41] and so on, all of which have good tensile strength and ductility. Jiang et al. [42] designed $Al_xNb_{0.5}TiV_2Zr_{0.5}$ alloy and explored the effect of Al on Laves phase precipitation. However, complex precipitates in lightweight high-entropy alloys can also restrict mechanical characteristic of the alloys. The precipitation of B2 and C14 phases in $Zr_{1.2}V_{0.8}Nb(Ti_xAl_y)$ LHEAs [33] system was successfully inhibited by controlling Al and Ti contents, and various LHEAs with good specific yield strength–plasticity combination were obtained.

In an effort to lower material density, Al and Ti elements are often taken into account by scholars as the main design elements for LHEAs [43, 44]. In the present study, we selected Ti, Zr, Nb, V, Cr, and Al elements to design a series of $(Ti_8Zr_6Nb_4V_5Cr_4)_{100-x}Al_x$ LHEAs with densities ranging from 5.79 to 6.22 g cm^{-3}. The vacuum non-self-consuming arc melting method is used to manufacture the alloy, which overcomes the related problems of traditional casting and sintering. The effect of Al content changes on the microstructure and mechanical properties of $(Ti_8Zr_6Nb_4V_5Cr_4)_{100-x}Al_x$ was investigated with different Al contents added, and the strengthening and plastic deformation mechanisms of the alloy were analyzed. In summary, LHEA materials have great potential for development.

2 Experimental

This study involves five $(Ti_8Zr_6Nb_4V_5Cr_4)_{100-x}Al_x$ (x = 0, 0.1, 0.2, 0.3, 0.4 at.%) LHEAs (referred to as LW-Alx) with different Al contents, named LW-Al0, LW-Al0.1, LW-Al0.2, LW-Al0.3, and LW-Al0.4, respectively. The nominal compositions of LW-Alx alloys are listed in Table 1. Subsequently, the raw materials are Ti, Zr, Nb, V, Cr and Al cylinder-shape particles with purity of 99.99 wt.% $(Ti_8Zr_6Nb_4V_5Cr_4)_{100-x}Al_x$ LHEAs button-type ingots were smelted by vacuum arc melting method under high purity argon atmosphere. Button ingots were obtained after melted 5 times to ensure uniform elemental distribution. The dimensional size of each ingot is about ϕ50 mm × 10 mm.

The specimens with a section size of 9 mm × 9 mm were cut off from the obtained ingots by a wire cutting

Table 1 Nominal compositions of $(Ti_8Zr_6Nb_4V_5Cr_4)_{100-x}Al_x$ LHEAs (at.%)

Alloy	Ti	Zr	Nb	V	Cr	Al
LW-Al0	29.63	22.22	14.81	18.52	14.82	–
LW-Al0.1	29.09	21.82	14.55	18.18	14.54	1.82
LW-Al0.2	28.57	21.43	14.29	17.86	14.28	3.57
LW-Al0.3	28.07	21.05	14.04	17.54	14.04	5.26
LW-Al0.4	27.59	20.69	13.79	17.24	13.79	6.90

machine. Cut-off specimens were mechanically abraded and polished with conventional metallographic preparation procedure. A D8 ADVANCE X-ray diffractometer (XRD) was applied to investigate phase constitutions of LW-Al*x* LHEAs. Microscopic morphologies of alloys were observed using a Zeiss SUPRA55 scanning electron microscope (SEM) with energy dispersive spectroscopy (EDS). Volume fractions of BCC and Laves phases were measured by image analysis software in backscattered electron (BSE) images. Grain sizes were measured by Image-Pro Plus software. The density of $(Ti_8Zr_6Nb_4V_5Cr_4)_{100-x}Al_x$ alloys with different additions of Al was tested by Archimedes Drainage method. Specimens of each alloy were measured for three times and the average was taken as density of the alloy. Microhardness of the polished surfaces was determined using an FM-ARS900 automatic microhardness tester with a load of 2.94 N for 15 s. The hardness of the alloys was tested at least five times with equal intervals and the average was taken as microhardness of each alloy. Three cylinders of ϕ4 mm × 6 mm were cut from each ingot as compression specimens. Compression tests were carried out at room temperature with a preliminary strain rate of 10^{-3} s^{-1} using an MTS 370 universal mechanical testing machine. To avoid accidental errors and get precise experimental data, each group of specimens was tested 3 times and the average value was calculated as the compressive strength and strain. After that, the compressive fracture morphologies of the alloys were observed in the secondary electron mode of SEM.

3 Results and discussion

3.1 Phase structure analysis

Figure 1 illustrates XRD analysis of $(Ti_8Zr_6Nb_4V_5Cr_4)_{100-x}Al_x$ (x = 0, 0.1, 0.2, 0.3, 0.4 at.%) LHEAs. Combined with scholars' studies of similar alloy compositions [45–48], it can be found that LW-Al0 alloy is composed of main phase of BCC phase and CrZrV-type C15 Laves phase. LW-Al0.1, LW-Al0.2, LW-Al0.3, and LW-Al0.4 alloys are composed of main phase BCC phase and ZrCrAl-type C14 Laves phase. Al addition into $Ti_8Zr_6Nb_4V_5Cr_4$ LHEA results in transformation from C15 Laves phase of LW-Al0 alloy to C14 Laves phase. It is noteworthy that the diffraction peak intensity values of C14 Laves phase are significantly higher than those of C15 Laves phase. Meanwhile, it can also be discovered from Fig. 1a that diffraction peaks of BCC phase lower than 40° in XRD pattern shift to higher 2θ (diffraction angle) and they get much wider with increase in Al content. Moreover, diffraction angle of the peaks increases gradually from 38.81° for LW-Al0 alloy to 39.67° for LW-Al0.4 alloy (Fig. 1b). The chief cause of the above phenomenon is construed as being related to the smaller atomic radius of Al atoms. The atomic radii of Ti, Zr, Nb, V, C, and Al are summarized in Table 2, where it can be found that the atomic radius of Al is 143 pm, but the difference with the atomic radius of Zr (160 pm) is still relatively large. The lattice constant of $(Ti_8Zr_6Nb_4V_5Cr_4)_{100-x}Al_x$ alloys decreases with increasing Al content, leading to increase in lattice distortion. Therefore, the phenomenon that peaks of BCC phase lower than 40° shift to a higher 2θ is consistent with the results obtained by XRD as displayed in Fig. 1.

3.2 Microstructure analysis

Figure 2 illustrates SEM-BSE images of $(Ti_8Zr_6Nb_4V_5Cr_4)_{100-x}Al_x$ (x = 0, 0.1, 0.2, 0.3, 0.4 at.%) LHEAs, and chemical composition of corresponding phases in the backscattered figure is displayed in Table 3. It can be found that LW-Al0 alloy without the addition of Al is composed of two phases, a light grey phase enriched with Ti and Nb (slightly enriched) elements, and a dark grey phase enriched with Zr, Cr, and V. The light grey phase is BCC structure, while the dark grey phase is C15 Laves structure, which corresponds to the results of XRD analysis. On the other aspect, LW-Al0 alloy forms a typical dendritic microstructure and dark grey C15 Laves phases with varying dimensions distributed at inter-dendritic area of BCC dendrites. The volume fractions of BCC phase and C15 Laves phase are 67% ± 3% and 33% ± 2%, respectively, as displayed in Fig. 2f (C15 Laves phase and C14 Laves phase collectively referred to as Laves).

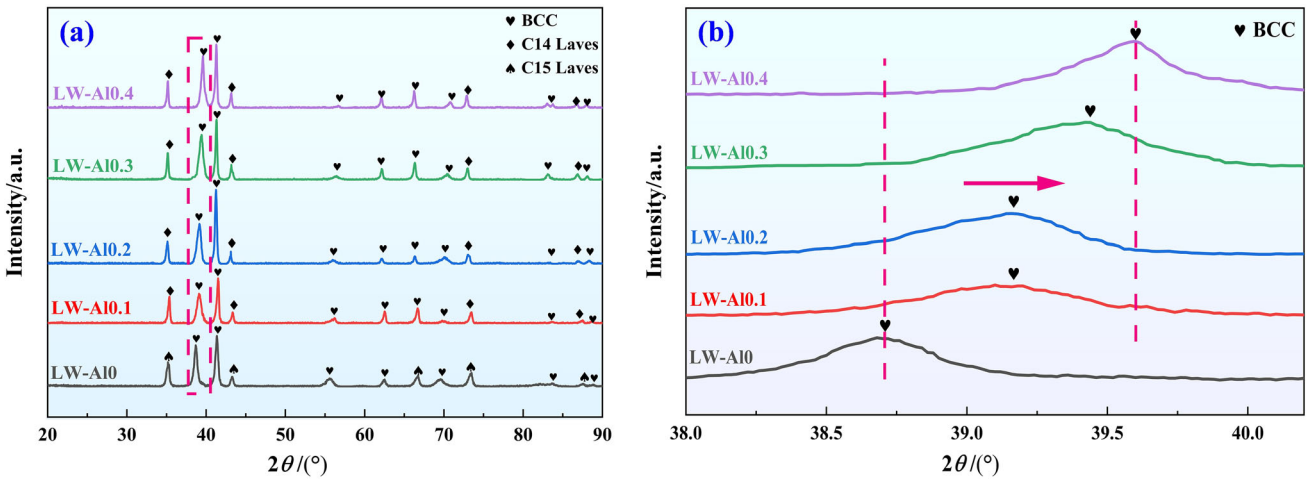

Fig. 1 XRD analysis of $(Ti_8Zr_6Nb_4V_5Cr_4)_{100-x}Al_x$ LHEAs (**a**) and diffraction peaks of BCC phase lower than 40° (**b**)

Table 2 Characteristics of elements in $(Ti_8Zr_6Nb_4V_5Cr_4)_{100-x}Al_x$ LHEAs system [16, 49, 50]

Element	Atomic mass/(g mol^{-1})	Melting point/°C	Density/(g cm^{-3})	Atomic radius/pm	Electronegativity
Ti	47.87	1668	4.51	145	1.54
Zr	91.22	1852	6.49	160	1.33
Nb	92.91	2468	8.57	146	1.59
V	50.94	1890	6.00	134	1.63
Cr	52.00	1907	7.19	124	1.66
Al	26.98	990	2.72	143	1.61

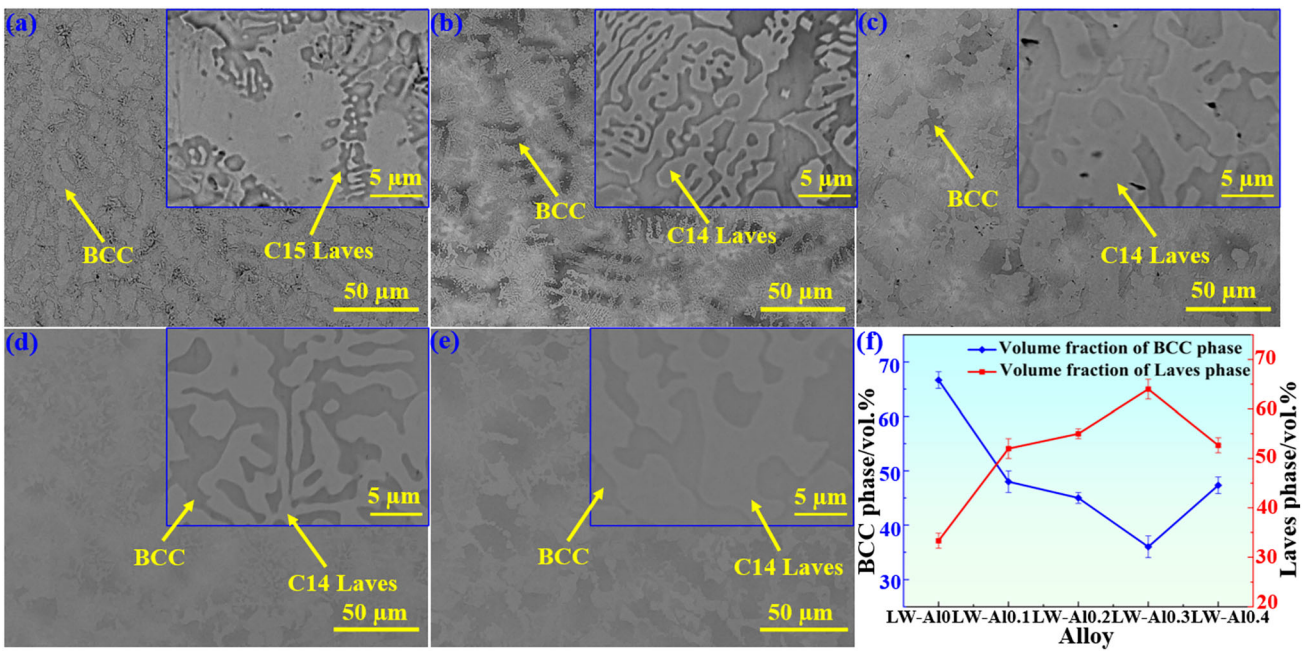

Fig. 2 SEM morphology of $(Ti_8Zr_6Nb_4V_5Cr_4)_{100-x}Al_x$ LHEAs. **a** LW-Al0; **b** LW-Al0.1; **c** LW-Al0.2; **d** LW-Al0.3; **e** LW-Al0.4; **f** volume fraction of BCC phase and Laves phase

Table 3 EDS results for typical region of $(Ti_8Zr_6Nb_4V_5Cr_4)_{100-x}Al_x$ LHEAs in Fig. 2 (at.%)

Alloy	Ti	Zr	Nb	V	Cr	Al
LW-Al0						
Nominal	29.63	22.22	14.81	18.52	14.82	–
Light grey phase (BCC)	40.25	20.31	16.32	17.30	5.82	–
Dark grey phase (C15 Laves)	19.13	24.22	12.90	19.89	23.86	–
LW-Al0.1						
Nominal	29.09	21.82	14.55	18.18	14.54	1.82
Dark phase (BCC)	38.98	15.31	22.08	16.25	6.15	1.23
Bright phase (C14 Laves)	19.52	28.32	7.02	20.13	22.59	2.42
LW-Al0.2						
Nominal	28.57	21.43	14.29	17.86	14.28	3.57
Dark phase (BCC)	36.12	14.97	23.65	15.27	7.02	2.97
Bright phase (C14 Laves)	21.42	27.65	5.07	20.15	21.54	4.17
LW-Al0.3						
Nominal	28.07	21.05	14.04	17.54	14.04	5.26
Dark phase (BCC)	35.23	13.06	24.73	14.69	8.23	4.06
Bright phase (C14 Laves)	20.91	28.86	3.75	20.93	18.85	6.70
LW-Al0.4						
Nominal	27.59	20.69	13.79	17.24	13.79	6.90
Dark phase (BCC)	34.65	12.76	23.98	14.63	8.57	5.41
Bright phase (C14 Laves)	20.43	28.62	3.61	19.95	19.01	8.38

Figure 2b–e shows microstructure morphology of LW-Al0.1, LW-Al0.2, LW-Al0.3, and LW-Al0.4 alloys, respectively. As shown in Fig. 2, the phase morphologies of LW-Al0.1, LW-Al0.2, LW-Al0.3, and LW-Al0.4 alloys are almost similar. These four alloys are still composed of two phases, namely, the dark phase enriched by Ti and Nb (slightly enriched) elements and the bright phase enriched by Zr, Cr, and Al (secondarily enriched) elements. The dark phase is also a BCC structure same as LW-Al0 alloy, and the bright phase is C14 Laves phase. Therefore, after addition of Al to the alloy, C15 Laves phase is transformed into C14 Laves phase, which corresponds to the XRD analysis results (Fig. 1). In addition, grain size distribution statistics of LW-Al*x* alloys are shown in Fig. 3. It can be seen that the grain size changes with increasing Al content. When the addition of Al is 0.3 at.%, the grains in LW-Al0.3 alloy are obviously refined, and the average grain size is 5.5 μm.

For Al-containing $(Ti_8Zr_6Nb_4V_5Cr_4)_{100-x}Al_x$ (x = 0.1, 0.2, 0.3, 0.4 at.%) LHEAs, phase structure of is significantly affected by Al content, and addition of Al transforms C15 Laves phase in LW-Al0 alloy to C14 Laves phase in other alloys (Fig. 2 and Table 3). The increase in Al content can lead to a slight increase in volume fraction of Laves phase in the alloy, except for LW-Al0.4 alloy. SEM images show that volume fractions of C14 Laves phase in LW-Al0.1, LW-Al0.2, LW-Al0.3 and LW-Al0.4 alloys are 52% ± 3%, 55% ± 2%, 64% ± 1% and 53% ± 2%, respectively. Obviously, the crystal structure and volume fraction of phases of fixed alloys are determined by chemical composition of alloys under certain equilibrium conditions [37, 51, 52]. The results show that Al content in $(Ti_8Zr_6Nb_4V_5Cr_4)_{100-x}Al_x$ alloys strongly influences the distribution between the two phases (BCC and Laves), and the volume fraction of the two phases in Al containing alloys is still varied.

Phase distribution of alloys with different additions of Al is varied for alloys with different phase compositions. The study of alloys with Laves phase can provide guidance for investigation of LW-Al*x* alloys with Al addition. For example, Al addition into the alloys with Laves phase can lead to transformation from C15 Laves phase into C14 Laves phase. As reported for Al–Cr–Nb alloys, the substitution of Al atoms occurs preferentially in sites dominated by Cr atoms in C14 lattice in the binary system. Then, Al atoms partially replace Cr element in the binary phase Cr_2Nb, resulting in the transformation of Laves phase from C15-type to C14-type [53].

3.3 Density and mechanical properties

The densities of $(Ti_8Zr_6Nb_4V_5Cr_4)_{100-x}Al_x$ (x = 0, 0.1, 0.2, 0.3, 0.4 at.%) LHEAs are shown in Table 4. Obviously, it can be found that the density of the alloys presents a declining tendency with increase in Al content. By

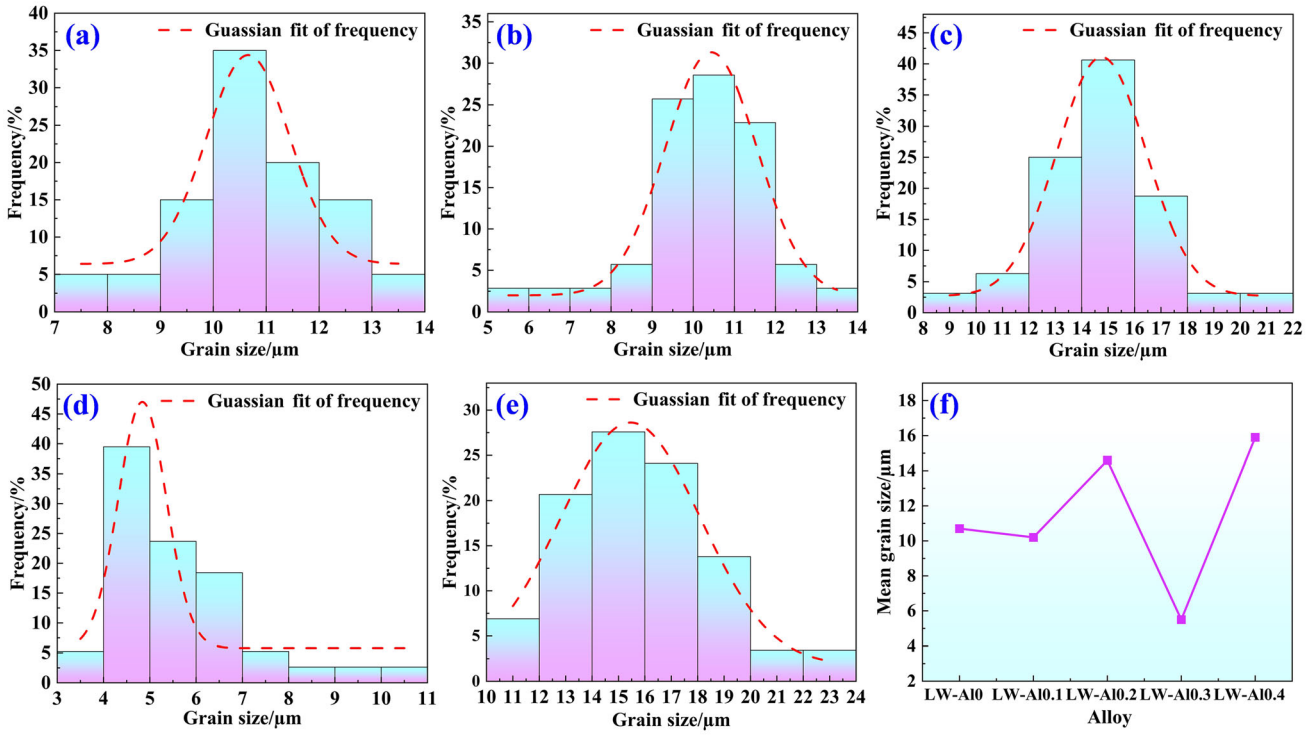

Fig. 3 Grain size of $(Ti_8Zr_6Nb_4V_5Cr_4)_{100-x}Al_x$ LHEAs. **a** LW-Al0; **b** LW-Al0.1; **c** LW-Al0.2; **d** LW-Al0.3; **e** LW-Al0.4; **f** average grain size of LW-Al*x*

Table 4 Density and strength of $(Ti_8Zr_6Nb_4V_5Cr_4)_{100-x}Al_x$ LHEAs

LHEA	Density/(g cm^{-3})	Yield strength/MPa	Microhardness/HV
LW-Al0	6.22 (± 0.875)	1536.5	535
LW-Al0.1	6.11 (± 0.653)	1780.9	598
LW-Al0.2	6.01 (± 0.852)	1803.1	669
LW-Al0.3	5.89 (± 0.981)	1921.2	738
LW-Al0.4	5.79 (± 0.679)	1812.2	671

Archimedes principle, the equation for measuring density of alloys is as follows,

$$\rho = \frac{m_1}{m_1 - m_3 + m_2} \times \rho_h \quad (1)$$

where ρ is density of alloy specimen to be tested; m_1 is mass of alloy specimen to be tested in air at room temperature; m_2 is mass of hanging wire in air at room temperature; m_3 is mass of alloy specimen to be tested submerged in distilled water suspended at room temperature; and ρ_h is density of distilled water. The results indicate that density of $(Ti_8Zr_6Nb_4V_5Cr_4)_{100-x}Al_x$ alloys decreases gradually with increase in Al element, from 6.22 ± 0.875 g cm^{-3} of LW-Al0 alloy to 5.79 ± 0.679 g cm^{-3} of LW-Al0.4 alloy.

Table 4 illustrates microhardness of $(Ti_8Zr_6Nb_4V_5Cr_4)_{100-x}Al_x$ (x = 0, 0.1, 0.2, 0.3, 0.4 at.%) LHEAs. The microhardness of LW-Al0 lightweight high entropy alloy is 535 HV, and microhardness of LW-Al0.1, LW-Al0.2 and LW-Al0.3 alloys is 598, 669, and 738 HV, respectively, indicating that increase in Al content has a slight influence on microhardness of alloys. And microhardness of LW-Al0.4 alloy is 671 HV. Figure 4a illustrates compressive stress–strain curves of LW-Al*x* alloys, which shows that yield strength ($\sigma_{0.2}$) of the alloys is increased and plasticity of the alloys is changed to various degrees with Al addition. Meanwhile, combining the yield strength values of the alloys listed in Table 4 (the yield strengths are expressed in 0.2% offset method), yield strength of LW-Al0 alloy is 1536.5 MPa. Subsequently, yield strengths of LW-Al0.1, LW-Al0.2, and LW-Al0.3 increase sequentially with the addition of Al, which are 1780.9, 1803.1, and 1921.2 MPa, respectively. However, yield strength value of LW-Al0.4

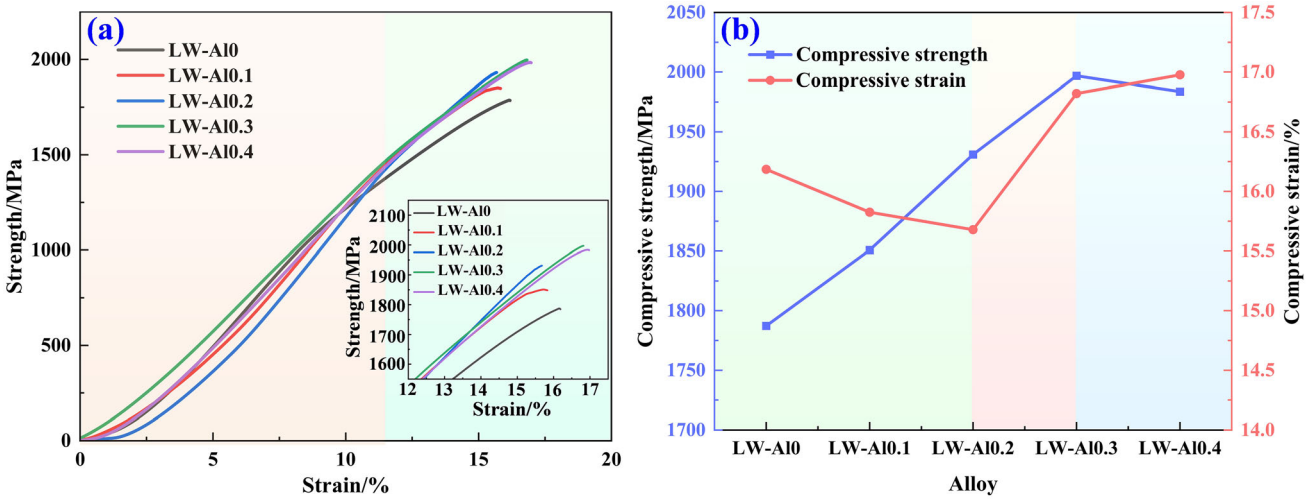

Fig. 4 Compressive properties of $(Ti_8Zr_6Nb_4V_5Cr_4)_{100-x}Al_x$ LHEAs. **a** Stress–strain diagram; **b** compressive strength stress diagram

with higher Al content decreases to 1812.2 MPa. Due to the addition of Al, the volume fraction of C14 Laves phase shows an increasing and then decreasing trend. The volume fraction of C14 Laves phase in LW-Al0.3 alloy reaches the maximum value, and meanwhile, the average grain size of LW-Al0.3 alloy is the smallest (Fig. 3). Moreover, it can be seen from Table 3 that with an increase in Al content, solid solution amount of Al atoms in C14 Laves phase increases significantly, which makes solid solution strengthening effect more obvious. Therefore, the yield strength of LW-Al0.3 alloy reaches the maximum value. Above all, yield strength of $(Ti_8Zr_6Nb_4V_5Cr_4)_{100-x}Al_x$ LHEAs is significantly affected by Al content. The phase volume fraction, grain refinement strengthening and solid solution of Al atoms give the best strength of LW-Al0.3 alloy.

Mechanical properties of high-entropy alloys are usually determined by typical compression tests and compression tests for LW-Al0, LW-Al0.1, LW-Al0.2, LW-Al0.3 and LW-Al0.4 alloys were conducted to systematically study influence of Al on microstructure and mechanical properties of lightweight high-entropy alloys. Al content was found to have a prominent effect on the strength and strain of LW-Al*x* alloys. As presented in Fig. 3, strength of the compression alloys shows a growing tendency toward the increase in Al content, and the fracture strain of LW-Al0.4 alloy achieves a maximum value of 16.98%. Results show that the addition of trace amounts of Al element has a significant effect on phase composition and microstructure of LW-Al*x* alloys. The volume fraction (Fig. 2f) of C14 Laves phase increases gradually with an increase in Al content, except for LW-Al0.4 alloy. The size of C14 Laves phase shows an overall expansion trend from LW-Al0.1 to LW-Al0.4 alloy, and the phase in LW-Al0.4 alloy is the largest. Compressive strength and strain of LW-Al0, LW-Al0.1, LW-Al0.2 alloys are 1787.3, 1850.8, 1930.9 MPa, and 16.19%, 15.83%, 15.68%, respectively. According to back-scattering diagrams and strain diagrams, the decrease trend of compressive strain is primarily accounted to the characteristics of C14 Laves phase itself. As is known to all, C14 Laves phase is hard and brittle, resulting volume fraction of C14 Laves phase in $(Ti_8Zr_6Nb_4V_5Cr_4)_{100-x}Al_x$ alloys is increased with an increase in Al content, and the size of Laves phase gradually expands, so that the hardness of the alloys is elevated, and strain shows a decreasing trend.

However, Figs. 2d and 3 demonstrate obvious grain refinement of $(Ti_8Zr_6Nb_4V_5Cr_4)_{100-x}Al_x$ alloys. As grain refinement can reduce grain size and increase interface area of alloys, the increase in grain boundary can prevent dislocation movement and therefore improve strength of alloys. As is well known, the increase in grain boundary can also prevent expansion of cracks and improve toughness of alloys. Concurrently, the refinement of grains will increase the number of grains and lead to uniform distribution of plastic deformation. Therefore, compressive strain and strength of LW-Al0.3 lightweight high-entropy alloy are all improved, and compressive strain and strength of the alloy reach 16.82% and 1996.9 MPa, respectively. From Figs. 2e and 3, it is found that grain size of LW-Al0.4 alloy increases obviously when the addition of Al is 0.4 at.%. The reduction in volume fraction of the hard and brittle Laves phase leads to a decrease in compressive strength and an increase in strain of LW-Al0.4 alloy at the same time. Therefore, the compressive strength of LW-Al0.4 alloy decreased to 1983.7 MPa, and the strain increased to 16.98%. Moreover, the solid solution of Al atoms in C14 Laves phase is the highest when Al content reaches 0.4 at.% as shown in Table 3, which indicates that doping of Al elements prevents precipitation of C14 Laves

phase in the alloy, thereby improving phase stability of the alloy and increasing strain of the alloy. In summary, the improvement of mechanical properties in LW-Alx alloys is the result of grain refinement strengthening, solid-solution strengthening of Al atoms, and second-phase precipitation strengthening, and thus LW-Al0.3 alloy shows the highest strength and better ductility performance.

3.4 Fracture morphology analysis

Fracture morphology of $(Ti_8Zr_6Nb_4V_5Cr_4)_{100-x}Al_x$ (x = 0, 0.1, 0.2, 0.3, 0.4 at.%) alloys after compression test was observed by secondary electron mode of SEM, and as shown in Fig. 5, LW-Al0 alloy without Al addition exhibits typical flat and bright river pattern morphologies, which is the main characteristic of the cleavage fracture. A small amount of dimple morphology and some tearing edges can also be observed on the fracture surface. The mixture of cleavage fracture with the dimple indicates that LW-Al0 alloy exhibits a typical quasi-cleavage fracture during the compression process, which is a type of brittle fracture.

LW-Al0.1 alloy exhibits flat and bright cleavage fracture morphology, as presented in Fig. 5b, indicating that the addition of Al can increase brittleness of the alloy. Additionally, some secondary cracks are also observed on the fracture surface, and the secondary cracks can disperse stresses caused by primary cracks during deformation of alloy and therefore improve yield strength of the alloys. Notably, yield strength of LW-Al0.1 alloy is increased by 15.9% compared with that of LW-Al0 alloy. In addition, fracture surface of LW-Al0.2 alloy with addition of Al by 0.2 at.% shows more cleavage fracture morphology, as presented in Fig. 5c, indicating significant brittleness increase in the alloy. Thus, fracture strain of LW-Al0.2 alloy is the lowest with minimum value of 15.68%. It can be interpreted that the solid solution amount of Al atoms in the alloy increases with more Al addition, and the strength of LW-Al0.2 alloy is enhanced due to solid solution strengthening. Moreover, the volume fraction of C14 Laves phase is increased by 0.2 at.% Al addition (as shown in Fig. 2f), and the hard and brittle nature of C14 Laves phase results in increased strength and decreased strain in LW-Al0.2 alloy. By increasing addition of Al content, obvious dimple morphology can be observed in Fig. 5d and e, and many concave or convex micro-pits were observed on fracture surface of LW-Al0.3 and LW-Al0.4 alloys. It is consistent with the ductility increase in LW-Al0.3 and LW-Al0.4 alloys shown in Fig. 4b and fracture strain of LW-Al0.4 alloy finally increases to 16.98%.

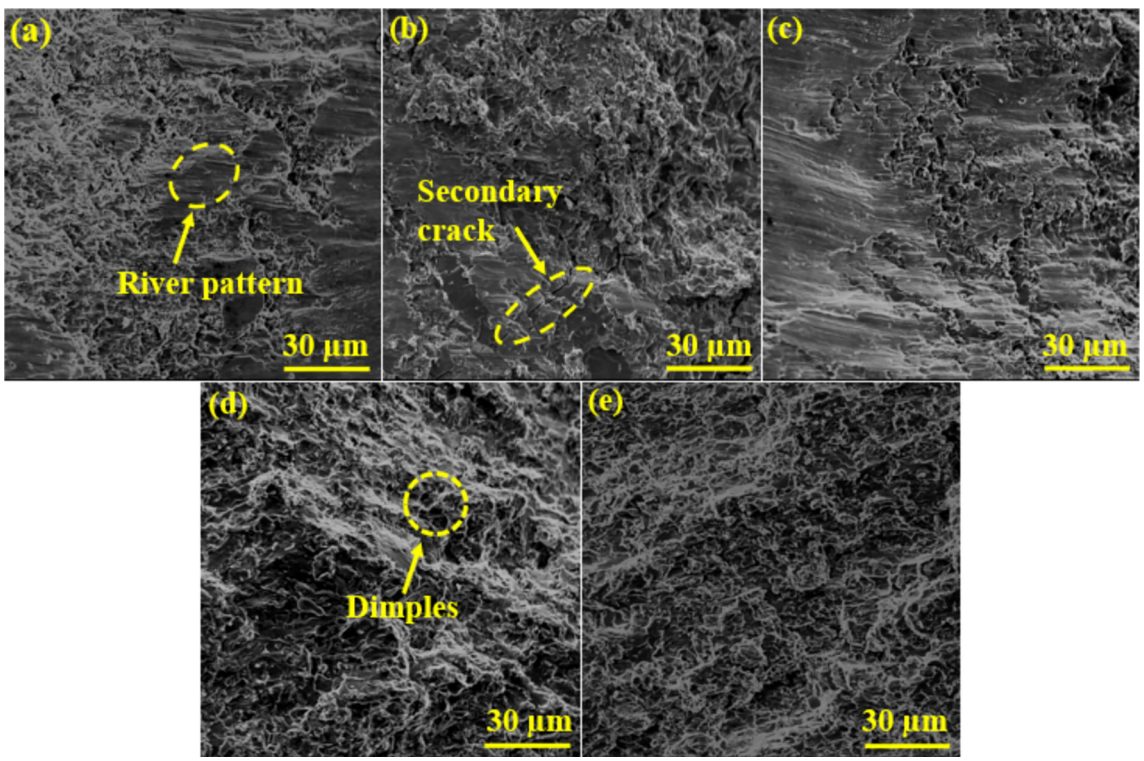

Fig. 5 Compression fracture morphology of $(Ti_8Zr_6Nb_4V_5Cr_4)_{100-x}Al_x$ LHEAs. **a** LW-Al0; **b** LW-Al0.1; **c** LW-Al0.2; **d** LW-Al0.3; **e** LW-Al0.4

4 Conclusions

1. $Ti_8Zr_6Nb_4V_5Cr_4$ (LW-Al0) lightweight high-entropy alloy is composed of BCC phase and C15 Laves phase, with volume fractions of 67% ± 3% and 33% ± 2%, respectively. C15 Laves phase of LW-Al0 alloy is transformed to C14 Laves phase in alloys with addition of Al, and BCC phase is significantly refined. Meanwhile, the volume fraction of C14 Laves phase increases with an increase in Al content. BCC phase and Laves phase are all significantly refined in LW-Al*x* alloy with Al content of 0.3 at.%.
2. The density of $(Ti_8Zr_6Nb_4V_5Cr_4)_{100-x}Al_x$ alloys decreases with an increase in Al content. When Al content in LW-Al*x* alloy increases from 0 to 0.4 at.%, the density of LW-Al0 and LW-Al0.4 alloys is decreased from 6.22 ± 0.875 to 5.79 ± 0.679 g cm^{-3}.
3. The compressive strength of LW-Al*x* alloy shows an increasing and then decreasing trend with an increase in Al content. And the compressive strength of LW-Al0.3 alloy with an Al content of 0.3 at.% reaches a maximum of 1996.9 MPa. The strength improvement of LW-Al*x* alloy is attributed to microstructure refinement, solid solution strengthening and precipitation of high-strength C14 Laves phase.
4. Fracture strain of LW-Al*x* alloy decreases first and then increases with an increase in Al, and the minimum is 15.68%. The ductility decrease of the alloys is related to the precipitation of brittle C14 Laves phase. However, fracture strain of the alloys with Al content higher than 0.3 at.% is increased, owing to grain refinement and reduction in volume fraction of C14 Laves phase, and fracture strain reaches the maximum of 16.98% with Al content of 0.4 at.%.

Acknowledgements This work was supported by National Natural Science Foundation of China (Grant No. 52001114), Program for Science and Technology Innovation Talents in Universities of Henan Province (No. 23HASTIT022 and 2021GGJS064), and Scientific Research Fund of State Key Laboratory of Materials Processing and Die and Mould Technology (Grant No. P2023-005).

Declarations

Conflict of interest No conflict of interest exits in the submission of this manuscript, and manuscript is approved by all authors for publication. I would like to declare on behalf of my coauthors that the work described was original research that has not been published previously, and not under consideration for publication elsewhere, in whole or in part. All the authors listed have approved the manuscript that is enclosed.

References

[1] M.H. Tsai, J.W. Yeh, Mater. Res. Lett. 2 (2014) 107–123.
[2] J. Cai, H. Zhang, L. Wang, X. Sun, X. Xu, X. Guo, D. Li, Mater. Sci. Eng. A 886 (2023) 145681.
[3] X. Yang, H. Fang, L. Zhou, Y. Tan, X. Ding, R. Chen, Mater. Sci. Eng. A 884 (2023) 145565.
[4] C. Monti, M. Turani, S. Wierschke, K. Papis, M. Bambach, Mater. Sci. Eng. A 892 (2024) 146035.
[5] H. Qi, Q.Y. Lv, G.H. Li, Y.D. Qu, R.M. Su, K.Q. Qiu, W. Zhang, B. Yu, Mater. Sci. Eng. A 878 (2023) 145183.
[6] C. Li, W. Fang, H. Yu, T. Peng, Z. Yao, W. Liu, X. Zhang, P. Xu, F. Yin, Mater. Sci. Eng. A 892 (2024) 146096.
[7] Z.H. Cao, G.Y. Zhai, Y.J. Ma, L.P. Ding, P.F. Li, H.L. Liu, H.M. Lu, Y.P. Cai, G.J. Wang, X.K. Meng, Int. J. Plast. 145 (2021) 103081.
[8] P.F. Li, Y.J. Ma, H. Ma, S.W. Ta, Z. Yang, X.T. Han, M.J. Kai, J.H. Chen, Z.H. Cao, J. Alloy. Compd. 895 (2022) 162574.
[9] Z. Cao, Y. Ma, Y. Cai, G. Wang, G. Pan, H. Ren, G. Zhai, Z. Zhang, P. Li, X. Meng, J. Alloy. Compd. 873 (2021) 159775.
[10] W. Zhang, Y. Zheng, F. Liu, D. Wang, F. Liu, C. Huang, Q. Li, X. Lin, W. Huang, Mater. Sci. Eng. A 820 (2021) 141537.
[11] Q. Xu, D.Z. Chen, C.R. Wang, W.C. Cao, Q. Wang, H.Z. Cui, S.Y. Zhang, R.R. Chen, Trans. Nonferrous Met. Soc. China 31 (2021) 512–520.
[12] Y. Shi, B. Yang, P.D. Rack, S. Guo, P.K. Liaw, Y. Zhao, Mater. Des. 195 (2020) 109018.
[13] W. Pan, P. Fu, Z. Li, H. Chen, Q. Tang, P. Dai, C. Liu, L. Lin, Intermetallics 144 (2022) 107523.
[14] P. Lyu, Q. Gao, T. Peng, H. Yuan, Q. Guan, J. Cai, H. Liu, X. Liu, Mater. Charact. 185 (2022) 111717.
[15] R. Feng, M. Gao, C. Lee, M. Mathes, T. Zuo, S. Chen, J. Hawk, Y. Zhang, P. Liaw, Entropy 18 (2016) 333.
[16] Q. Zhi, X. Tan, Z. Liu, Y. Liu, Q. Zhang, Y. Chen, M. Li, Micron 144 (2021) 103031.
[17] F. Stein, A. Leineweber, J. Mater. Sci. 56 (2021) 5321–5427.
[18] B. Gludovatz, A. Hohenwarter, D. Catoor, E.H. Chang, E.P. George, R.O. Ritchie, Science 345 (2014) 1153–1158.
[19] J. Miao, C.E. Slone, T.M. Smith, C. Niu, H. Bei, M. Ghazisaeidi, G.M. Pharr, M.J. Mills, Acta Mater. 132 (2017) 35–48.
[20] A.P.M. de Araujo, C.S. Kiminami, V. Uhlenwinkel, P. Gargarella, Mater. Sci. Eng. A 886 (2023) 145670.
[21] O.N. Senkov, G.B. Wilks, J.M. Scott, D.B. Miracle, Intermetallics 19 (2011) 698–706.
[22] Q. Xu, Q. Wang, D.Z. Chen, Y.A. Fu, Q.S. Shi, Y.J. Yin, S.Y. Zhang, China Foundry 19 (2022) 495–502.
[23] O. El-Atwani, N. Li, M. Li, A. Devaraj, J.K.S. Baldwin, M.M. Schneider, D. Sobieraj, J.S. Wróbel, D. Nguyen-Manh, S.A. Maloy, E. Martinez, Sci. Adv. 5 (2019) eaav2002.
[24] O. Maulik, D. Kumar, S. Kumar, S.K. Dewangan, V. Kumar, Mater. Res. Express 5 (2018) 052001.
[25] G. Zhang, W. Ma, P. Ji, B. Zhang, X. Zhang, J. Zhang, X. Zhang, M. Ma, R. Liu, Mater. Sci. Eng. A 885 (2023) 145602.
[26] J. Zhou, J. Zhang, C. Hu, Y. Liu, Z. Ma, C. Song, Q. Zhai, Mater. Sci. Eng. A 874 (2023) 145088.
[27] S. Lee, J. Moon, H. Kim, Y.H. Cho, H.H. Lee, H. Choi, Y. Kim, D.W. Suh, K. Jeong, H.N. Han, Mater. Sci. Eng. A 891 (2024) 146003.
[28] G.H. Gu, J.H. Lee, H. Kwon, H.S. Kim, Mater. Sci. Eng. A 893 (2024) 146132.
[29] A. Kumar, M. Gupta, Metals 6 (2016) 199.
[30] R. Li, J.C. Gao, K. Fan, Mater. Sci. Forum 650 (2010) 265–271.
[31] Y. Jia, Y. Jia, S. Wu, X. Ma, G. Wang, Materials 12 (2019) 1136.
[32] R. Li, X. Li, J. Ma, Y. Zhang, Intermetallics 121 (2020) 106780.
[33] L. Wang, S. Chen, B. Li, T. Cao, B. Wang, L. Wang, Y. Ren, J. Liang, Y. Xue, Mater. Sci. Eng. A 814 (2021) 141234.
[34] K. Gao, Y. Chu, W. Zhou, Y. Tian, Y. Zhang, Y. Li, J. Mater. Sci. Technol. 150 (2023) 124–137.

[35] Y. Qiu, Y.J. Hu, A. Taylor, M.J. Styles, R.K.W. Marceau, A.V. Ceguerra, M.A. Gibson, Z.K. Liu, H.L. Fraser, N. Birbilis, Acta Mater. 123 (2017) 115–124.
[36] N.Y. Yurchenko, N.D. Stepanov, S.V. Zherebtsov, M.A. Tikhonovsky, G.A. Salishchev, Mater. Sci. Eng. A 704 (2017) 82–90.
[37] N.D. Stepanov, N.Y. Yurchenko, V.S. Sokolovsky, M.A. Tikhonovsky, G.A. Salishchev, Mater. Lett. 161 (2015) 136–139.
[38] W. Kai, C.C. Liao, I.R. Yang, C.I. Chu, S.F. Liu, J.J. Kai, Corros. Sci. 211 (2023) 110890.
[39] H. Wang, W. Chen, C. Chu, Z. Fu, Z. Jiang, X. Yang, E.J. Lavernia, Mater. Sci. Eng. A 885 (2023) 145661.
[40] Y. Chen, Z. Xu, M. Wang, Y. Li, C. Wu, Y. Yang, Mater. Sci. Eng. A 792 (2020) 139774.
[41] N.Y. Yurchenko, N.D. Stepanov, D.G. Shaysultanov, M.A. Tikhonovsky, G.A. Salishchev, Mater. Charact. 121 (2016) 125–134.
[42] W. Jiang, Y. Wang, X. Wang, B. Jiang, T. Ma, H. Kang, D. Zhu, Mater. Sci. Eng. A 865 (2023) 144628.
[43] Z. Peng, B. Li, Z. Luo, X. Chen, Y. Tang, G. Yang, P. Gong, Materials 16 (2023) 2922.
[44] X. Huang, J. Miao, A.A. Luo, Scripta Mater. 210 (2022) 114462.
[45] O.N. Senkov, S.V. Senkova, D.B. Miracle, C. Woodward, Mater. Sci. Eng. A 565 (2013) 51–62.
[46] O.N. Senkov, S.V. Senkova, C. Woodward, D.B. Miracle, Acta Mater. 61 (2013) 1545–1557.
[47] N.Y. Yurchenko, N.D. Stepanov, A.O. Gridneva, M.V. Mishunin, G.A. Salishchev, S.V. Zherebtsov, J. Alloy. Compd. 757 (2018) 403–414.
[48] I.I. Gorbachev, V.V. Popov, A. Katz-Demyanetz, V. Popov, E. Eshed, Phys. Metals Metallogr. 120 (2019) 378–386.
[49] S. Guo, C.T. Liu, Prog. Nat. Sci. Mater. Int. 21 (2011) 433–446.
[50] T. Xu, Q. Chen, L. Ji, Z. Zheng, K. Wang, H. Liu, J. Alloy. Compd. 956 (2023) 170179.
[51] N.D. Stepanov, N.Y. Yurchenko, D.G. Shaysultanov, G.A. Salishchev, M.A. Tikhonovsky, Mater. Sci. Technol. 31 (2015) 1184–1193.
[52] N.D. Stepanov, D.G. Shaysultanov, G.A. Salishchev, M.A. Tikhonovsky, Mater. Lett. 142 (2015) 153–155.
[53] O. Prymak, F. Stein, J. Alloy. Compd. 513 (2012) 378–386.